JACS
JOURNAL OF THE AMERICAN CHEMICAL SOCIETY
Article
pubs.acs.org/JACS

Synergistic Effects in Bimetallic Palladium–Copper Catalysts Improve Selectivity in Oxygenate Coupling Reactions

Konstantinos A. Goulas,[†,‡,§,#,○] Sanil Sreekumar,[†,§,∇,○] Yuying Song,[∥] Purnima Kharidehal,[∥,⊗] Gorkem Gunbas,[†,§,×] Paul J. Dietrich,[⊥] Gregory R. Johnson,[‡] Y. C. Wang,[⊥] Adam M. Grippo,[§] Lars C. Grabow,[*,∥] Amit A. Gokhale,[§,⊥,+] and F. Dean Toste[*,†,§]

[†]Department of Chemistry, University of California, Berkeley, California 94720, United States
[‡]Department of Chemical and Biomolecular Engineering, University of California, Berkeley, California 94720, United States
[§]Energy Biosciences Institute, University of California, Berkeley, California 94720, United States
[∥]Department of Chemical and Biomolecular Engineering, University of Houston, Houston, Texas 77204, United States
[⊥]BP North America, Naperville, Illinois 60563, United States

Supporting Information

ABSTRACT: Condensation reactions such as Guerbet and aldol are important since they allow for C–C bond formation and give higher molecular weight oxygenates. An initial study identified Pd-supported on hydrotalcite as an active catalyst for the transformation, although this catalyst showed extensive undesirable decarbonylation. A catalyst containing Pd and Cu in a 3:1 ratio dramatically decreased decarbonylation, while preserving the high catalytic rates seen with Pd-based catalysts. A combination of XRD, EXAFS, TEM, and CO chemisorption and TPD revealed the formation of CuPd bimetallic nanoparticles with a Cu-enriched surface. Finally, density functional theory studies suggest that the surface segregation of Cu atoms in the bimetallic alloy catalyst produces Cu sites with increased reactivity, while the Pd sites responsible for unselective decarbonylation pathways are selectively poisoned by CO.

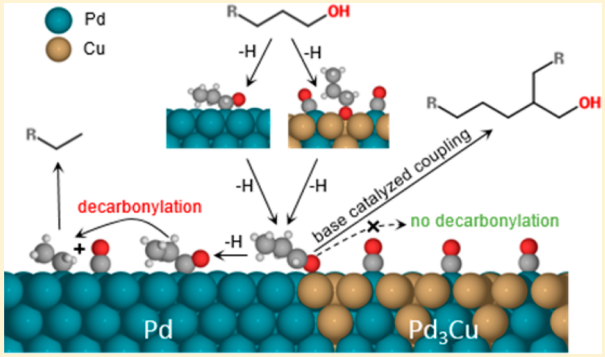

INTRODUCTION

The Guerbet and related condensation reactions[1] have the potential to provide a broadly applicable platform for the production of higher molecular weight aliphatic alcohols and carbonyl compounds from short-chain oxygenates (Scheme 1). Such compounds find use in a wide range of applications including plasticizers, lubricants, fuels, fuel additives, and personal care products. Consequently, a variety of heterogeneous[2−4] and homogeneous[5−7] transition metal catalysts have been developed for these transformations. Of particular interest is the application of these reactions for producing bio-based fuels and chemicals.[8] Recently, we reported the use of such condensation reactions as part of a strategy for combining fermentation and chemical upgrading to yield biodiesel precursor molecules.[9] In this sequence, sugars were fermented to a mixture of acetone, butanol, and ethanol (ABE) that was upgraded to heavier ketones through Guerbet and aldol condensation.

High selectivity and moderate yields have been achieved for the Guerbet reaction employing homogeneous metal-based catalysts.[5−7] The heterogeneous versions of this chemistry, however, require suppression of the decarbonylation[10] and/or esterification (Tishchenko) reactions[11] inherent to metal oxide-supported transition metal-catalyzed processes operating at elevated temperatures. Herein, we report that catalysts composed of palladium–copper impregnated on a hydrotalcite–carbon (HT-C) functional support[12] suppress these side reactions, and through a combination of characterization

Scheme 1. Condensation Reactions of Alcohols[a]

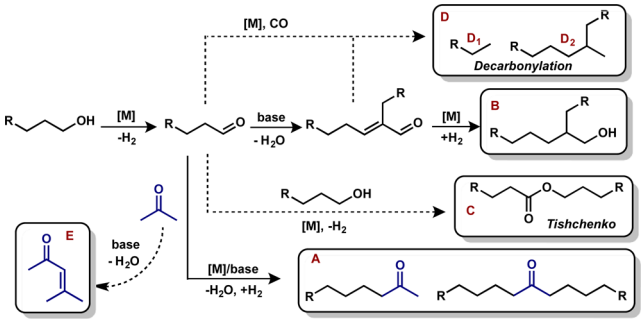

[a]Solid arrows indicate desired reactions; dashed arrows indicate undesired reactions.

Received: March 3, 2016
Published: May 19, 2016

ACS Publications © 2016 American Chemical Society

DOI: 10.1021/jacs.6b02247
J. Am. Chem. Soc. 2016, 138, 6805–6812

and first-principles studies, we provide insights into the link between catalyst properties and the improved selectivity.

MATERIALS AND METHODS

Catalyst Preparation. Synthetic hydrotalcite was obtained from Sigma-Aldrich and was calcined at 823 K for 4 h (1 K min^{-1} ramp). Subsequently, an aqueous (unless otherwise noted) solution of the appropriate metal precursor was added dropwise to the resulting metal oxide to the point of incipient wetness. The solids were dried in ambient air at 368 K for 20 h and were subsequently calcined for 4 h at 823 K (5 K min^{-1} ramp). In Table S1, the precursors and the pretreatment gas are shown for the individual catalysts. All catalysts contained 2 wt% transition metal.

Carbon-based catalysts were prepared by incipient wetness impregnation of $La(NO_3)_3{\cdot}6H_2O$, $Mg(NO_3)_2{\cdot}6H_2O$, and $Al(NO_3)_3{\cdot}6H_2O$ onto activated carbon (Fisher Scientific, 50−200 mesh, 05-690A), to obtain a 2.9% oxide loading After drying at 368 K for 20 h, the catalyst was treated under He flow (100 mL min^{-1}) for 4 h at 773 K (ramp rate 5 K min^{-1}).

Palladium and copper were added to the treated solids by incipient wetness impregnation, using aqueous Pd and Cu nitrate solutions. The impregnated solids were dried at 368 K and were subsequently treated in flowing He for 4 h at 773 K (ramp rate 5 K min^{-1}).

Catalyst Characterization. The structure of the catalysts was investigated by X-ray diffraction (XRD) and X-ray absorption spectroscopy (XAS). XRD experiments were performed using a Bruker D8 instrument using a $2\theta-\theta$ geometry, scanning from $2\theta = 20°$ to 60°, at a rate of 0.02 deg/s. XAS experiments were performed at the Advanced Photon Source, Argonne National Laboratory (Argonne, IL). The bending magnet and insertion device beamlines on Sector 10 were used for the experiments. Spectra were recorded at the Pd K (24 350 eV) and Cu K (8979 eV) edges, in transmission (Pd and Cu) or fluorescence (Cu) detection modes. Three flow-through ion chambers were used as detectors, measuring the incident and transmitted radiation through the sample and through a reference foil.

In the transmission experiments, samples were packed in a 6-well sample holder diluted with boron nitride as a binder to form self-supporting pellets. Sample loading was calculated to give an absorbance (μ_x) of <2.5, and an edge step ($\Delta\mu_x$) between 0.2 and 1.5. Self-supporting pellets were pressed and held in a custom fluorescence holder that held the sample at a 45° angle incident to the beam path. The detector was placed at a right angle with respect to the beam path.

The XAS data were processed using the Athena and Artemis programs of the Demeter suite. The EXAFS oscillations were fitted simultaneously for the Cu and Pd edges from $R = 1.4$ to 3.2 and for $k = 2.5$ to 12.

Temperature-programmed desorption (TPD) experiments were conducted in an AutoChem 2920 automated flow chemisorption unit (Micromeritics, Norcross, GA), equipped with a thermal conductivity detector (TCD). In these experiments, 150 mg of catalyst was supported on a quartz wool plug in a U-shaped tube. The catalyst was reduced at 523 K for 1 h (5 K min^{-1} ramp) and was cooled down to 313 K. Next, 10% CO/He gas was pulsed until no further adsorption of CO was detected in the TCD. Subsequently, the temperature was raised at 5 K min^{-1} to 1073 K under a He flow while monitoring the TCD signal.

For the TEM experiments, holey carbon film grids were used, with nylon (for the PdCu/HT) and Au grids (for the PdCu/HT-C). STEM-EDS images were collected at 80 kV (PdCu/HT) or 200 kV (PdCu/HT-C) and the concentrations of elements quantified using the Cliff-Lorimer method.

Catalytic Reaction Procedures. Gas-phase reactions were conducted in a plug-flow reactor. The reactor tube was made of fused silica, and the catalyst was supported on a quartz frit (12.7 mm o.d.). All catalysts were sieved down to a size under 0.18 μm, to avoid mass transfer effects. Prior to reaction, the catalysts were reduced in a 50% H_2/He mixture at 523 K for 1 h (ramp rate 5 K min^{-1}). The reactor was enclosed in a clamshell furnace (Applied Test Systems, Butler, PA) with aluminum inserts, and the temperature was controlled by a PID controller (Watlow, Burlington, VT).

Gas flow through the catalyst was regulated via mass flow controllers (Parker). Liquid reactants (ethanol:acetone:butanol = 1:3:6 by mass, corresponding to 1:2.3:3.7 by moles, all obtained from Sigma-Aldrich) was injected into the gas stream through a syringe port in the heated transfer lines using a Legato 100 syringe pump.

The products of the reaction were analyzed online using a gas chromatograph (Shimadzu GC 2014) equipped with a flame ionization detector and an HP-1 capillary column. Rates reported herein are calculated by averaging at least four chromatograms at identical conditions, after 2 h of steady state operation.

Identification of the products was achieved by the injection of standard compounds and, for the ones that were unavailable, by GC/MS, as described below.

Prior to batch reactions, the catalysts that were pretreated in air or He were reduced at 773 K for 2 h under a hydrogen flow (100 mL/min, ramp 2 K min^{-1}). Reactions were conducted in pressure tubes (Q-Tubes, Qlabtech, Inc.), using a procedure described in detail elsewhere.[13] In a typical experiment, 390 mg of octanol as a reactant, 300 mg of catalyst (corresponding to 7.2 mg of metal), and 75 mg of dodecane as internal standard were added to a QTube, which was sealed and heated to 503 K for 18 h. The product was diluted with tetrahydrofuran or toluene, and an aliquot was analyzed by GC/MS, using a Varian CP-3800 GC/MS with two VF-5ms columns (Agilent Technologies), connected to a flame ionization detector and a triple-quadrupole mass spectrometer.

Theoretical Calculation Methods. All periodic density functional theory (DFT) calculations were done using the Vienna ab initio Simulation Package (VASP) as electronic structure calculator in the atomic simulation environment (ASE).[14−16] Exchange and correlation were described by the PW91 generalized gradient approximation (GGA-PW91)[17,18] within the projector-augmented-wave (PAW) method.[19,20] A dipole correction was applied in the direction normal to the surface.[21] The Fermi temperature was set to $k_BT = 0.1$ eV, and the resulting electronic energies were extrapolated to 0 K.[21,22] No zero point energy or entropy corrections were added. The cutoff energy for expanding the wave function into plane wave basis functions was set to 400 eV. Geometries were considered converged when the force was below 0.05 eV/Å.

The optimized bulk lattice constants obtained using a 11×11×11 k-point set are 3.989 Å for Pd and 3.646 Å for Cu, which are in good agreement with the experimental values of 3.890 and 3.615 Å, respectively.[23] For the Pd_3Cu bulk alloy the calculated lattice constant is 3.891 Å. All surfaces were modeled as four layer slabs with the top two layers fully relaxed and the bottom two layers fixed to the bulk truncated positions. For $fcc(111)$ surfaces we used a periodic (4×4) unit cell to accommodate the larger C_3 hydrocarbons and match the 3:1 ratio of the Pd_3Cu alloy. To test possible Cu segregation models, we considered one $fcc(211)$ surface in a (4×1) unit cell. For all surface models the vacuum distance between slabs in the normal direction was set to be 20 Å. A Monkhorst−Pack k-point mesh of (4×4×1) is used to sample the Brillouin zone.[24]

The reported adsorption energies are calculated with reference to the clean surface and the gas-phase energies of propanol, H_2, and CO. Negative values correspond to exothermic adsorption. The d-band center of specific catalyst surface atoms is calculated as the first moment of the atom projected local density of d-states referenced to the Fermi level. We use the d-band center position to assess the reactivity of metal surfaces according to the d-band model by Nørskov and Hammer.[25,26] Transition states were located using the climbing image nudged elastic band algorithm with a resolution of at least five intermediate images per elementary reaction step.[27,28] All transition states are true saddle points in the potential energy surface as confirmed by a single imaginary frequency along the reaction path. Frequency analysis was performed in the harmonic oscillator approximation using a Cartesian displacement of 0.01 Å.

DOI: 10.1021/jacs.6b02247
J. Am. Chem. Soc. 2016, 138, 6805−6812

Table 1. Product Selectivity for ABE Condensation in Gas Phase[a]

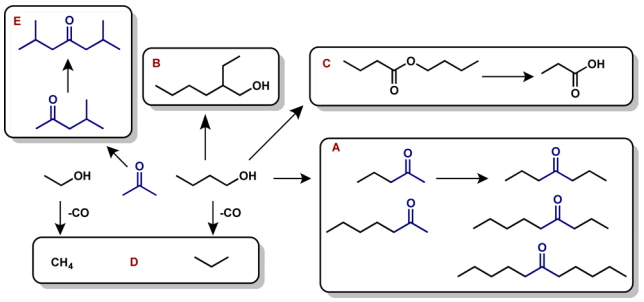

	product selectivity (%)[b]						
catalyst	A	B	C	D	E	condensation:decarbonylation ratio	rate[c] (μmol·g cat^{-1}·ks^{-1})
Cu/HT	74	1.1	0	0	24	>99	50
Pd/HT	72.8	8.1	0.3	16.8	2.2	5.3	58
Pd/HT-C	68.3	0.2	1.5	21.2	8.9	6.9	91
PdCu/HT	74.0	3.5	0.2	19.8	2.5	3.6	145
PdCu/HT-C	68.3	5.1	0.8	4.3	2.3	49	148

[a]Reaction conditions: gas-phase flow reactor, temperature = 473 K, total pressure = 101.3 kPa, WHSV = 2.1 h^{-1}; feed, 3.6 kPa ethanol:acetone:butanol mixture (1:2.3:3.7 molar ratio), balance He. [b]Products: **A**, 2-pentanone, 2-heptanone, 4-nonanone, 6-undecanone, and the corresponding alcohols; **B**, 2-ethyl-1-hexanol and 2-ethylhexanal; **C**, butyl butyrate and butyric acid; **D**, methane, propane, and hexane; **E**, isovalerone and methyl isobutyl ketone. [c]Rate is defined as moles of acetone converted to the desired products normalized by total mass of catalyst. Total conversion <10%.

RESULTS AND DISCUSSION

The condensation reaction of ABE was studied in a gas-phase plug-flow reactor. Catalyst screening (Table S2) showed that Pd-based catalysts were quite active, although significant decarbonylation to alkanes (**D**) under our reaction conditions meant poor selectivity for the desired condensation routes to products **A** and **B**. While switching to a catalyst composed of 3:1 Pd:Cu[29] impregnated on hydrotalcite (HT) resulted in a significant improvement in the reaction rate, it did not improve the selectivity toward the desired condensation chemistry. However, supporting this bimetallic catalyst on a mixed hydrotalcite/carbon support produced a dramatic improvement in the condensation to decarbonylation ratio (Table 1), while maintaining the higher reaction rate seen on the PdCu/HT catalyst.

Similar alloying and support effects on the selectivity were observed during the solution phase Guerbet condensation of 1-octanol (Table 2). In the absence of a ketone such as acetone, the most likely condensation product is that derived from the Guerbet reaction (**B**). Table 2, entry 2 illustrates that in addition to this product, the Pd/HT-catalyzed reaction produced significant amounts of decarbonylated byproducts ($\mathbf{D_1}$ and $\mathbf{D_2}$, i.e., C_7 and C_{15} alkanes, respectively) as well as some ester product (**C**). In contrast, decarbonylation products were minimal on the Cu/HT catalyst; however, the Tishchenko reaction to form the ester (**C**) was favored over the desired condensation reaction on this catalyst (Table 2, entry 1). An attempt to alloy Pd and Cu into the PdCu/HT catalyst gave similar conversion as Pd/HT albeit with marginally improved selectivity for the Guerbet reaction (Table 2, entry 3 vs 2). Finally, in line with the gas-phase studies, the use of bimetallic PdCu impregnated on 2.9 wt% HT-C completely suppressed decarbonylation and minimized ester formation (Table 2, entry 5).

The location of Cu atoms in the catalyst and their oxidation state give interesting insights to explain these observations. Based on the XAS data of PdCu/HT (Figure 1A,B) a

Table 2. Product Selectivity in the 1-Octanol Guerbet Reaction in the Liquid Phase[a]

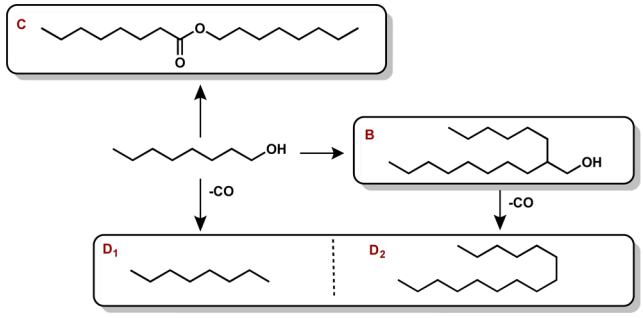

entry	catalyst (0.9 mol%)	conv (%)	B:D_2	B:D_1	B:C
1	Cu/HT	34	>99:1	>99:1	0.45:1
2	Pd/HT	34	0.67:1	1.8:1	4.2:1
3	PdCu/HT	37	1.1:1	1:1	4.3:1
4	Pd/HT-C	12	3.9:1	4.7:1	2.8:1
5	PdCu/HT-C	50	>99:1	>99:1	7:1

[a]Reaction conditions: batch reactions with 1-octanol (3 mmol), metal-HT (300 mg), metal:octanol = 0.019 mol/mol, temperature = 503 K, time = 3 h. Conversion and selectivity determined by calibrated internal standard (*n*-dodecane).

significant fraction of Cu exists as Cu^{2+}, forming a ternary Cu−Mg−Al oxide.[30] The shape of the white line, reminiscent of the octahedral hexaaquocopper complex ion, is consistent with the conclusion that in this material Cu^{2+} ions are octahedrally coordinated, presumably replacing Mg^{2+} and Al^{3+} in the HT structure. Replacement of Mg and Al in HT structures by first-row[31] and second-row[31,32] transition metals has been widely reported and also accounts for the small amount of oxidation of Pd (Figure 1A). This situation renders a significant fraction of the Cu unavailable for alloying with Pd. Conversely, on the carbon-supported catalysts, Cu is fully reduced (Figure 1D) and preferentially alloys with Pd because of the chemical mismatch between the covalent solid carbon

DOI: 10.1021/jacs.6b02247
J. Am. Chem. Soc. 2016, 138, 6805−6812

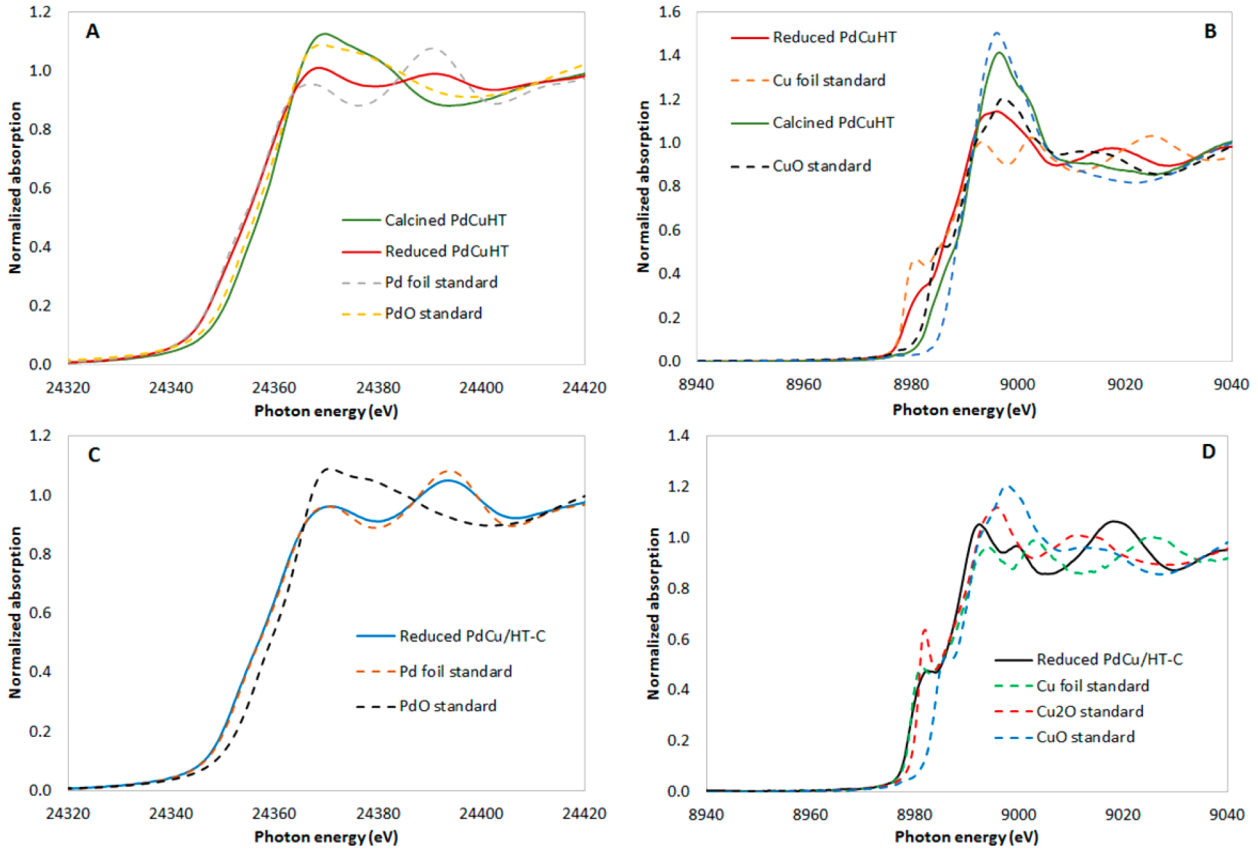

Figure 1. XANES of the Pd edge (A) and the Cu edge (B) of a PdCu/HT catalyst and a PdCu/HT-C catalyst (C, Pd edge, and D, Cu edge).

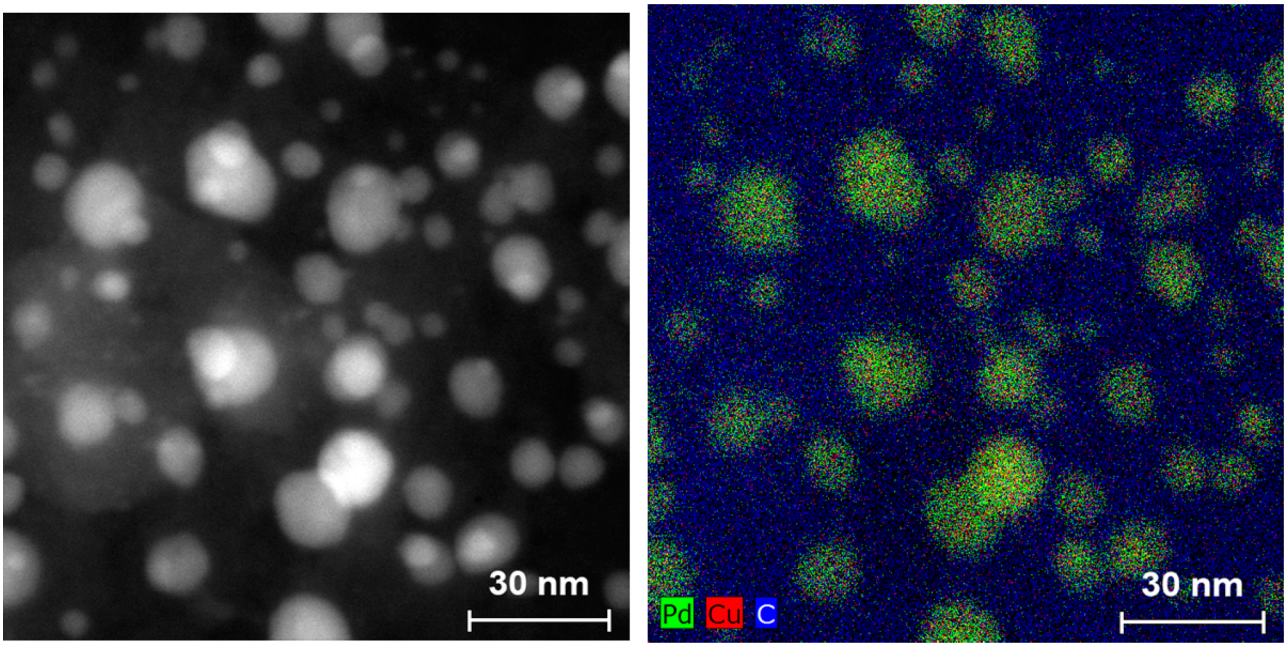

Figure 2. TEM images of the PdCu/HT-C catalyst. Left: HAADF-STEM image. Right: STEM-EDS elemental maps for Pd, Cu, and C.

and the Cu cations. We hypothesize that this alloy formation suppresses the decarbonylation reaction and is responsible for the increased selectivity.

To further understand the interactions between Pd and Cu and confirm the alloy formation on the PdCu/HT-C catalyst, we conducted transmission electron microscopy (TEM) studies, which demonstrated that Pd and Cu were collocated (Figure 2). This contrasts with observations of the PdCu/HT catalyst, in which the Cu is not alloyed with the Pd, but is distributed in the support (Figure S1). Our XANES analysis of the PdCu/HT catalyst also showed that Cu^{2+} ions substitute into the Mg–Al oxide matrix (Figure S2), consistent with this observation.

DOI: 10.1021/jacs.6b02247
J. Am. Chem. Soc. 2016, 138, 6805–6812

Fitting of the EXAFS at the Cu and Pd edges showed the presence of mixed Pd-Cu and Cu-Pd scattering, providing further evidence for alloy formation in the PdCu/HT-C sample. More specifically, Pd has a significantly higher total coordination number of 11.9 compared to 9.8 for Cu, suggesting segregation of Cu atoms to the surface of the metal nanoparticles (Table 3).[33,34] CO chemisorption at 313 K on the Pd/HT-C catalyst (average particle size of 24 nm estimated by XRD) measured a 0.5:1 CO:surface metal ratio, consistent with literature reports of CO binding on monometallic Pd surfaces.[35] The same measurement showed a CO:surface metal ratio of 0.24:1 for the PdCu/HT-C catalyst (16 nm particles by XRD). This measurement is consistent with a mixed Pd/Cu surface, as Cu does not bind CO above 300 K.[36]

Table 3. Fitting of the EXAFS of the PdCu/HT-C Catalyst, where *d* Is Distance, *N* Is Coordination Number, and E_0 Is the Energy Offset

Pd edge		Cu edge	
$d_{Pd\text{-}Cu}$ (Å)	2.645 ± 0.005	$d_{Cu\text{-}Pd}$ (Å)	2.645 ± 0.005
$d_{Pd\text{-}Pd}$ (Å)	2.724 ± 0.003	$d_{Cu\text{-}Cu}$ (Å)	2.597 ± 0.017
$N_{Pd\text{-}Pd}$	9.043 ± 0.426	$N_{Cu\text{-}Cu}$	2.214 ± 0.997
$N_{Pd\text{-}Cu}$	2.839 ± 0.431	$N_{Cu\text{-}Pd}$	7.556 ± 0.632
Pd-Pd σ^2	75 ± 4	Cu-Cu σ^2	71 ± 5
Pd-Cu σ^2	91 ± 12	Cu-Pd σ^2	91 ± 12
E_0 (eV)	−9.80 ± 0.37	E_0 (eV)	3.96 ± 0.47

DFT calculations were conducted in order to gain further insights into the observed reactivity trends for the alloy catalysts. Pd(111) and Cu(111) surfaces were used to understand the reactivity on Pd- and Cu-based catalysts. On the other hand, to select the most representative model for the bimetallic PdCu catalyst, several models with various amounts of Cu surface segregation were evaluated, and their agreement with EXAFS, XRD, and TPD results was assessed. In addition, we also calculated the CO binding energy and C−O stretch frequency, $\nu_{C=O}$, for the bulk terminated $Pd_3Cu(111)$, four Pd/Cu near surface alloy surfaces with Cu enrichment on the (111) facet, and a (211) step model with Cu atoms preferentially occupying exposed step sites. All models are depicted in Figure S3, and the CO adsorption characteristics are provided in Table S4. Of all these surface representations, a composite of Pd_3Cu bulk alloy with the top surface enriched in Cu to give a $PdCu_3/Pd_3Cu(111)$ surface alloy was determined to be most accurate based on the evidence from the characterization studies. For example, CO TPD on the alloy catalyst showed a decrease in the number of strong binding sites, but with an associated shift to stronger binding (Figure S4). When compared with Pd(111), the $PdCu_3/Pd_3Cu(111)$ model surface also showed a 0.15 eV stronger binding of CO on top of the exposed Pd atoms, while the Cu surface atoms bind CO considerably weaker. Notably, the step site model can be excluded, because the calculated $\nu_{C=O}$, 1493 cm^{-1}, was well below the experimental value, and the fraction of step sites on particles with 16 nm diameter is insignificant.

To evaluate the impact of alloy formation on reactivity and product selectivity, while keeping the problem computationally tractable, the reaction was studied using 1-propanol as the probe molecule. Mechanistically, the reaction begins with sequential abstractions of two hydrogen atoms from alcohol on the metal particles to give aldehyde, followed by the aldol condensation reaction on the support material or the undesired decarbonylation reaction on the metal surface. Initial insights into catalytic activity of the metal catalyzed steps can be gained by the comparison of the potential energy diagrams shown in Figure 3. Two competing pathways are considered for four

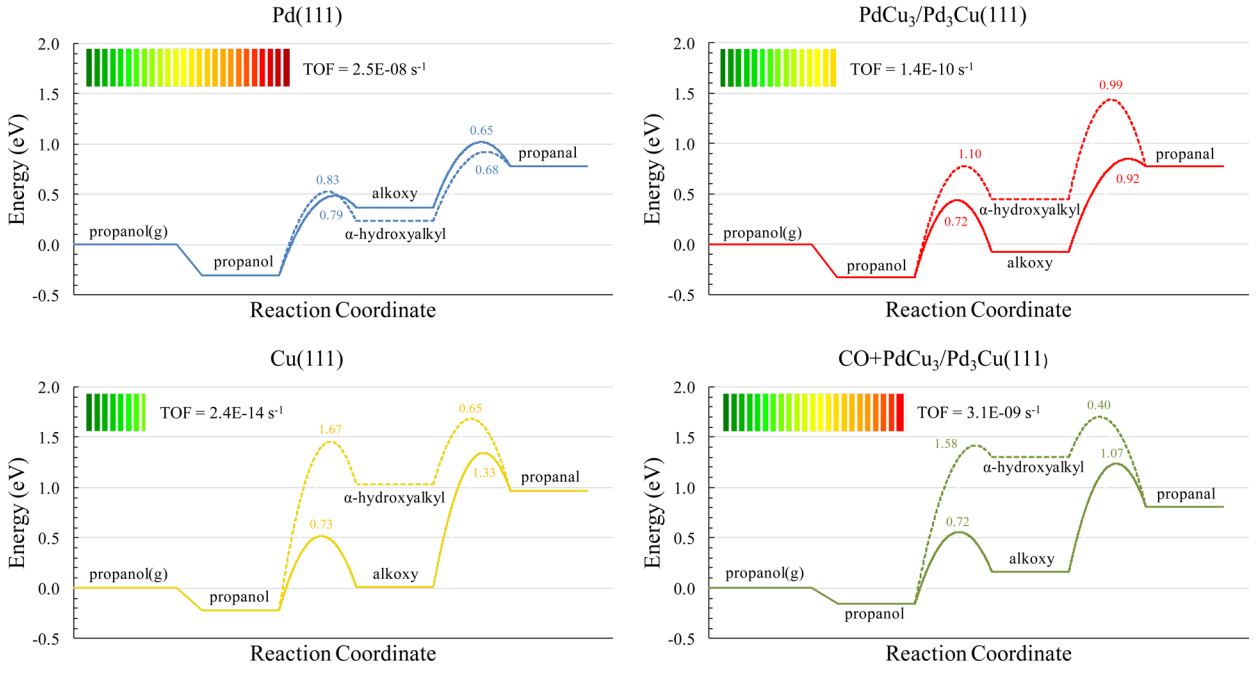

Figure 3. Potential energy diagrams for the metal catalyzed sequential dehydrogenation of propanol to propanal. The solid lines correspond to the O-bound alkoxy intermediate ($CH_3CH_2CH_2O$), whereas the dashed lines refer to the stability of the C-bound α-hydroxyalkyl intermediate (CH_3CH_2CHOH). The horizontal bar illustrates a turnover frequency (TOF) estimate in logarithmic scale from a microkinetic model at 503 K, 0.9 bar propanol, and 0.1 bar CO.

DOI: 10.1021/jacs.6b02247
J. Am. Chem. Soc. 2016, 138, 6805−6812

catalyst models: Pd(111), Cu(111), $PdCu_3/Pd_3Cu(111)$, and a CO-modified $CO+PdCu_3/Pd_3Cu(111)$, i.e., the $PdCu_3/Pd_3Cu$-(111) surface with Pd sites blocked by CO. The first pathway drawn with solid lines proceeds via the O-bound alkoxy intermediate after an initial O−H cleavage step, whereas the second pathway is initiated by a C−H scission step to form the C-bound α-hydroxyalkyl intermediate.

A visual inspection of the potential energy diagrams suggests that the alkoxy intermediate provides the lower energy pathway for pure Cu and the $PdCu_3/Pd_3Cu$ alloy model. For the pure Pd surface both pathways are competitive. This interpretation is confirmed by a 6-step microkinetic model for the steady-state dehydrogenation of propanol to propanal via both competing pathways at T = 503 K and P = 1 bar. The elementary steps of this model are

$$RCH_2OH(g) + * \rightleftharpoons RCH_2OH* \quad (I)$$

$$RCH_2OH* \rightleftharpoons RCH_2O* + {}^1/_2H_2 \quad (II)$$

$$RCH_2OH* \rightleftharpoons RCHOH* + {}^1/_2H_2 \quad (III)$$

$$RCH_2O* \rightleftharpoons RCHO* + {}^1/_2H_2 \quad (IV)$$

$$RCHOH* \rightleftharpoons RCHO* + {}^1/_2H_2 \quad (V)$$

$$RCHO* \rightleftharpoons RCHO(g) + * \quad (VI)$$

where * represents a surface site and X* denotes the adsorbed species X. We stress that this microkinetic model is not intended to quantitatively reproduce the experimental data. It should rather be understood as a tool to aid the analysis of the potential energy diagrams in Figure 3. Additional output from the microkinetic model is summarized in Table S5.

For a pure propanol feed the turn over frequency (TOF) for Pd(111) is 3 orders of magnitude higher than for the $PdCu_3/Pd_3Cu(111)$ alloy and 11 orders of magnitude higher than for Cu(111). In the context of the experimental results in Tables 1 and 2, this result is not realistic. To reconcile the difference, we also consider the reversible adsorption of CO, the product of the unselective decarbonylation pathway, as step (VII) in the microkinetic model. CO is known to bind strongly to Pd and can poison the catalyst.

$$CO(g) + * \rightleftharpoons CO* \quad (VII)$$

The addition of competitive CO adsorption strongly reduces the rate on Pd(111) and $PdCu_3/Pd_3Cu(111)$, whereas the rate on Cu(111) is insensitive up to 10% CO in the feed. This is purely a site-blocking phenomenon as the CO coverage on Cu(111) remains negligible, but CO completely saturates the surface of Pd(111) and the Pd sites of $PdCu_3/Pd_3Cu(111)$. This is consistent with the CO TPD results, which show CO desorbing from Pd/HT-C and Pd_3Cu/HT-C at temperatures higher than the reaction temperature of 503 K. Therefore, a more representative model for the Pd_3Cu alloy catalyst is one which tracks this CO poisoning effect explicitly. Thus, we considered a modified model with CO adsorbed on the strong binding Pd sites of the $PdCu_3/Pd_3Cu(111)$ surface, i.e., $CO+PdCu_3/Pd_3Cu(111)$, shown in Figure 4 (bottom).

The $CO+PdCu_3/Pd_3Cu(111)$ surface is equally insensitive to further CO poisoning just as the pure Cu(111) surface. A comparison of the TOF for propanal formation over Pd(111) and $CO+PdCu_3/Pd_3Cu(111)$ in the presence of 10% CO

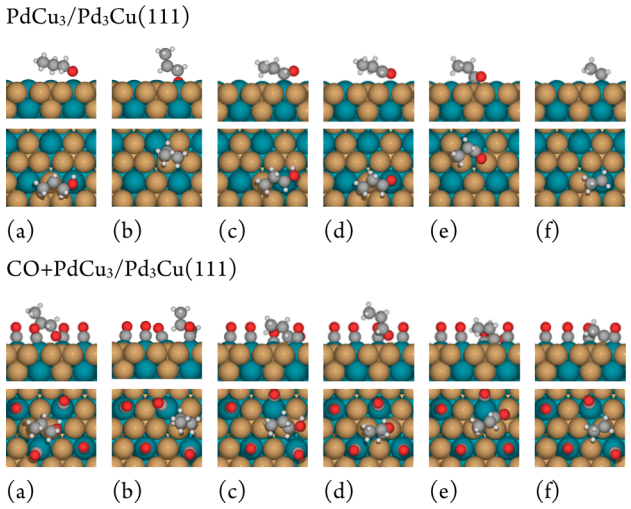

Figure 4. Side and top views of the most favorable adsorption geometries on Cu-rich $PdCu_3/Pd_3Cu(111)$ (upper) and CO-poisoned CO + $PdCu_3/Pd_3Cu(111)$ (lower) model surfaces. The adsorbates from left to right are (a) propanol ($CH_3CH_2CH_2OH$), (b) alkoxy ($CH_3CH_2CH_2O$), (c) α-hydroxyalkyl (CH_3CH_2CHOH), (d) propanal (CH_3CH_2CHO), (e) ethylacylium (CH_3CH_2CO), and (f) ethyl (CH_3CH_2).

indicates comparable activity of the two models. This is particularly remarkable because all binding on $CO+PdCu_3/Pd_3Cu(111)$ occurs on Cu sites, which showed ca. 5 orders of magnitude lower activity. This phenomenon is consistent with the experimentally observed activity increase for PdCu alloy catalysts (Tables 1 and 2). The TOF in the presence of 10% CO for all model surfaces is depicted at horizontal bar in logarithmic scale in Figure 3.

The inset of Figure 5 shows the relative positons of the d-band centers of surface metal atoms on the Pd, Cu, and PdCu

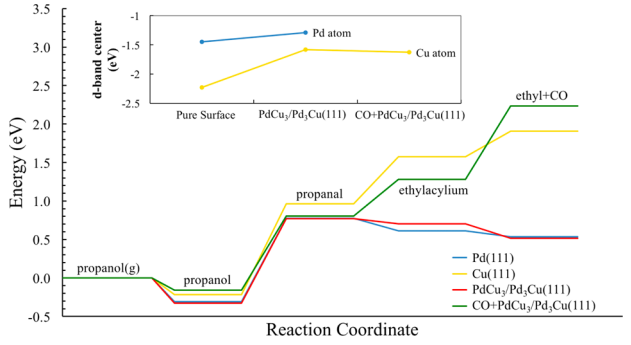

Figure 5. Thermodynamic potential energy diagram of metal catalyzed steps occurring during the initial phase of the Guerbet reaction and decarbonylation. Energies are reported with respect to the clean surface, propanol, CO, and hydrogen. The inset shows the d-band center position with respect to the Fermi level of the clean Pd(111) and Cu(111) surfaces, and the Pd or Cu atoms of the PdCu alloy models.

catalysts as modeled by Pd(111), Cu(111), and $PdCu_3/Pd_3Cu(111)$. The d-band center of Pd(111) is closer to the Fermi level, and Pd(111) is expected to bind species generally more strongly than Cu(111).[25,26,38] The $PdCu_3/Pd_3Cu(111)$ model surface exhibits a unique electronic structure, in which the d-band center position of both the surface Cu (e_d = −1.58 eV) and Pd (e_d = −1.29 eV) atoms move closer to the Fermi

DOI: 10.1021/jacs.6b02247
J. Am. Chem. Soc. 2016, 138, 6805−6812

level when compared to the monometallic Cu(111) (e_d = −2.23 eV) and Pd(111) (e_d = −1.45 eV) reference surfaces. Notably, the upshift of the *d*-band center is more pronounced for the Cu atoms, rendering them nearly as reactive as the monometallic Pd(111) surface. Indeed, the red line in Figure 5 representing the stability of reaction intermediates on the Cu-rich $PdCu_3/Pd_3Cu(111)$ alloy surface by and large coincides with the blue line representing species on pure Pd(111). Furthermore, the *d*-band center upshift and associated activity increase of the exposed Cu atoms on $PdCu_3/Pd_3Cu(111)$ are reflected in the higher TOF obtained from the microkinetic model compared to Cu(111).

The work by İnoğlu and Kitchin suggests that the presence of CO should result in a modification of the *d*-band structure of the surrounding metal atoms.[39] Their model applies to the particular case of $PdCu_3/Pd_3Cu(111)$, where the CO modification causes a small downshift of the *d*-band center of the adjacent surface Cu atoms (inset in Figure 5), while completely blocking access to the Pd atoms. This situation should result in small changes, i.e., little coverage effect, for intermediates chemisorbing to Cu sites, but intermediates binding to Pd sites should experience a significant destabilization. From the geometries for $PdCu_3/Pd_3Cu(111)$ in Figure 4 we can classify α-hydroxyalkyl, ethylacylium, and ethyl as C-bound species that preferentially bind to available Pd surface atoms of the $PdCu_3/Pd_3Cu(111)$ alloy. Indeed, the potential energy diagram for $CO+PdCu_3/Pd_3Cu(111)$ shown in green in Figure 3 confirms this expectation. In the presence of CO the C-bound α-hydroxyalkyl intermediate (Figure 4) must now bind to a less favorable Cu site and becomes highly unstable. In contrast, the O-bound alkoxy intermediate, which preferentially adsorbs to Cu, is only mildly destabilized in the presence of CO. The strong destabilization of α-hydroxyalkyl has no negative impact on the activity of $CO+PdCu_3/Pd_3Cu(111)$, because the dominant reaction pathway proceeds along the alkoxy intermediate (Table S5).

While the role of the metals is to catalyze the dehydrogenation steps to yield aldehydes, the aldol condensation reaction is carried out by the base support, i.e. hydrotalcite, and so is virtually independent of the metals used. The effect of the metal surfaces on selectivity is then due to the competing metal-catalyzed decarbonylation reaction, specifically the stability of key reaction intermediates on mono- and bimetallic Pd, Cu, and PdCu surfaces. To this end, Figure 5 summarizes the thermodynamic stability of key intermediates formed along the decarbonylation pathway. These data are tabulated in Table S6. The corresponding binding geometries on the clean and CO-blocked $PdCu_3/Pd_3Cu(111)$ models are provided in Figure 4, with results for the monometallic Pd(111) and Cu(111) surfaces included as Figure S5.

The unselective decarbonylation reaction is initiated by hydrogen-abstraction from the α-carbon of propanal to give a C-bound ethylacylium intermediate (CH_3CH_2CO) that subsequently yields the undesired ethyl species (CH_3CH_2) following the elimination of the CO group. Since a slow decarbonylation step leads to high aldol coupling selectivity by suppressing the major side reaction, the higher observed selectivity of the condensation reaction compared to decarbonylation on Cu can be rationalized using the potential energy diagram in Figure 5. The highly endothermic formation of the ethylacylium and ethyl intermediates on Cu during decarbonylation prevents the reaction from following this pathway. In contrast, these intermediates form readily on Pd, favoring the undesired side reaction.

On clean $PdCu_3/Pd_3Cu(111)$, the products of decarbonylation, ethylacylium and ethyl, bind via their carbon atom to exposed Pd sites in exothermic steps suggesting this reaction to be just as facile on the alloy surface as it is on the Pd(111). If we, however, consider the realistic possibility of Pd site blocking by CO, the modified $CO+PdCu_3/Pd_3Cu(111)$ model surface also offers an explanation for the high selectivity for the Guerbet reaction. Because the intermediates ethylacylium and ethyl bind through their C atoms and their favored binding site on Pd atoms is blocked by CO, they must bind on Cu sites where the formation of these intermediates is thermodynamically unfavorable. In fact, Figure 5 indicates that their formation on $CO+PdCu_3/Pd_3Cu(111)$ (green) is even more endothermic than on the Cu(111) surface (yellow). Consequently, the undesired decarbonylation pathway is less accessible. If ethyl were to displace the CO molecule on the Pd site, moving CO to a Cu site, then the co-adsorption of these two species is 0.11 eV less stable. With this observation our conclusion regarding the effect of CO site blocking on coupling selectivity holds also for other surface arrangements as long as Pd atoms are the minority species on the surface and surrounded by active Cu atoms, a hypothesis with strong support from the characterization results.

CONCLUSIONS

In summary, the Pd_3Cu alloy combines the activity of Pd with the selectivity of Cu. We explain this phenomenon by proposing a segregated Pd_3Cu surface model with a Cu-rich surface. Under reaction conditions, the exposed Pd sites are blocked by CO. The formation of the Pd_3Cu alloy raises the *d*-band center of Cu significantly, leading to increased reactivity of Cu for the dehydrogenation reaction, but does not provide favorable binding sites for decarbonylation intermediates that bind through their carbon atoms. The suppression of the decarbonylation reaction is consistent with the high selectivity toward the base-catalyzed Guerbet and ABE coupling reactions observed experimentally. Thus, even with large excess of Pd in the catalyst, the catalytic centers are surface Cu atoms with a modified electronic structure due to interactions with Pd.

ASSOCIATED CONTENT

Supporting Information

The Supporting Information is available free of charge on the ACS Publications website at DOI: 10.1021/jacs.6b02247.

Additional reaction and characterization data, including Tables S1−S6 and Figures S1−S19 (PDF)

AUTHOR INFORMATION

Corresponding Authors

*grabow@uh.edu

*fdtoste@berkeley.edu

Present Addresses

#K.A.G.: CCEI, University of Delaware, Newark, DE 19716

∇S.S.: Dow Chemical Co., Midland, MI 48640

⊗P.K.: Aspen Tech, Inc., Houston, TX 77042

×G.G.: METU, Fen-Edebiyat Fakültesi Kimya Bolumu, 06800 Ankara, Turkey

+A.A.G.: BASF Corp., 33 Wood Avenue South, Iselin, NJ 08830

Author Contributions

○K.A.G. and S.S. contributed equally to this work.

DOI: 10.1021/jacs.6b02247
J. Am. Chem. Soc. 2016, 138, 6805−6812

Notes

The authors declare no competing financial interest.

■ ACKNOWLEDGMENTS

This work was funded by the Energy Biosciences Institute. Y.S., P.K., and L.C.G. acknowledge financial support by the U.S. Department of Energy (DOE), Office of Science, Office of Basic Energy Sciences, under award number DE-SC0011983. The authors also thank Prof. J. T. Miller, Prof. J. R. Long, Dr. S. Sankaranarayanapillai, Dr. A. Getsoian, Dr. E. R. Sacia, Dr. M. Kulzick, and Mr. J. Chen for useful discussions and their collaboration. The authors thank the personnel at the Materials Research Collaborative Access Team (MRCAT) for their help in X-ray absorption experiments. MRCAT operations are supported by the DOE and the MRCAT member institutions. This research used resources of the Advanced Photon Source, a U.S. Department of Energy Office of Science User Facility, operated for the DOE Office of Science by Argonne National Laboratory under Contract No. DE-AC02-06CH11357. This research used resources of the National Energy Research Scientific Computing (NERSC) Center, a DOE Office of Science User Facility, supported by the Office of Science, U.S. Department of Energy, under contract number DE-AC02-05CH11231. Additional computational resources were provided through the Extreme Science and Engineering Discovery Environment (XSEDE), which is supported by National Science Foundation (No. ACI5681053575). We also acknowledge the use of the Maxwell/Opuntia Cluster and advanced support from the Center of Advanced Computing and Data Systems (CACDS) at the University of Houston, facilitated under NSF-MRI Grant No. ACI-1531814, to carry out the research presented here. Last, we acknowledge instrument time at the National Center for Electron Microscopy (NCEM), part of the Molecular Foundry. Work at the Molecular Foundry was supported by the Office of Science, Office of Basic Energy Sciences, U.S. Department of Energy, under Contract No. DE-AC02-05CH11231.

■ REFERENCES

(1) Kozlowski, J. T.; Davis, R. J. *ACS Catal.* **2013**, *3*, 1588−1600.
(2) Carlini, C.; Macinai, A.; Marchionna, M.; Noviello, M.; Raspolli Galletti, A. M.; Sbrana, G. *J. Mol. Catal. A: Chem.* **2003**, *206*, 409−418.
(3) Carlini, C.; Flego, C.; Marchionna, M.; Noviello, M.; Raspolli Galletti, A. M.; Sbrana, G.; Basile, F.; Vaccari, A. *J. Mol. Catal. A: Chem.* **2004**, *220*, 215−220.
(4) Carlini, C.; Di Girolamo, M.; Macinai, A.; Marchionna, M.; Noviello, M.; Raspolli Galletti, A. M.; Sbrana, G. *J. Mol. Catal. A: Chem.* **2003**, *204*−*205*, 721−728.
(5) Dowson, G. R. M.; Haddow, M. F.; Lee, J.; Wingad, R. L.; Wass, D. F. *Angew. Chem., Int. Ed.* **2013**, *52*, 9005−9008.
(6) Matsu-ura, T.; Sakaguchi, S.; Obora, Y.; Ishii, Y. *J. Org. Chem.* **2006**, *71*, 8306−8308.
(7) Gregorio, G.; Pregaglia, G. F.; Ugo, R. *J. Organomet. Chem.* **1972**, *37*, 385−387.
(8) (a) Corma, A.; Iborra, S.; Velty, A. *Chem. Rev.* **2007**, *107*, 2411−2502. (b) Alonso, D. M.; Bond, J. Q.; Dumesic, J. A. *Green Chem.* **2010**, *12*, 1493−1513. (c) Goulas, K. A.; Toste, F. D. *Curr. Opin. Biotechnol.* **2016**, *38*, 47−53.
(9) (a) Anbarasan, P.; Baer, Z. C.; Sreekumar, S.; Gross, E.; Binder, J. B.; Blanch, H. W.; Clark, D. S.; Toste, F. D. *Nature* **2012**, *491*, 235−239. (b) Sreekumar, S.; Baer, Z. C.; Gross, E.; Padmanaban, S.; Goulas, K.; Gunbas, G.; Alayoglu, S.; Blanch, H. W.; Clark, D. S.; Toste, F. D. *ChemSusChem* **2014**, *7*, 2445−2448. (c) Balakrishnan, M.; Sacia, E. R.; Sreekumar, S.; Gunbas, G.; Gokhale, A. A.; Scown, C. D.; Toste, F. D.; Bell, A. T. *Proc. Natl. Acad. Sci. U. S. A.* **2015**, *112*, 7645−7649.
(10) Sitthisa, S.; Resasco, D. E. *Catal. Lett.* **2011**, *141*, 784−791.
(11) Inui, K.; Kurabayashi, T.; Sato, S.; Ichikawa, N. *J. Mol. Catal. A: Chem.* **2004**, *216*, 147−156.
(12) (a) Winter, F.; van Dillen, A. J.; de Jong, K. P. *Chem. Commun.* **2005**, 3977−3979. (b) Winter, F.; Koot, V.; van Dillen, A. J.; Geus, J. W.; de Jong, K. P. *J. Catal.* **2005**, *236*, 91−100.
(13) Sreekumar, S.; Baer, Z. C.; Pazhamalai, A.; Gunbas, G.; Grippo, A.; Blanch, H. W.; Clark, D. S.; Toste, F. D. *Nat. Protoc.* **2015**, *10*, 528−537.
(14) Kresse, G.; Furthmüller, J. *Comput. Mater. Sci.* **1996**, *6*, 15−50.
(15) Kresse, G.; Furthmüller, J. *Phys. Rev. B: Condens. Matter Mater. Phys.* **1996**, *54*, 11169−11186.
(16) Bahn, S. R.; Jacobsen, K. W. *Comput. Sci. Eng.* **2002**, *4*, 56−66.
(17) Perdew, J. P.; Chevary, J. A.; Vosko, S. H.; Jackson, K. A.; Pederson, M. R.; Singh, D. J.; Fiolhais, C. *Phys. Rev. B: Condens. Matter Mater. Phys.* **1992**, *46*, 6671−6687.
(18) White, J. A.; Bird, D. M. *Phys. Rev. B: Condens. Matter Mater. Phys.* **1994**, *50*, 4954−4957.
(19) Blöchl, P. E. *Phys. Rev. B: Condens. Matter Mater. Phys.* **1994**, *50*, 17953−17979.
(20) Kresse, G.; Joubert, D. *Phys. Rev. B: Condens. Matter Mater. Phys.* **1999**, *59*, 1758−1775.
(21) Bengtsson, L. *Phys. Rev. B: Condens. Matter Mater. Phys.* **1999**, *59*, 12301−12304.
(22) Gillan, M. J. *J. Phys.: Condens. Matter* **1989**, *1*, 689−711.
(23) King, H. W. In *CRC Handbook of Chemistry and Physics*; Haynes, W. M., Bruno, T. J., Lide, D. R., Eds.; CRC Press: New York, 2015; pp 15−18.
(24) Monkhorst, H. J.; Pack, J. D. *Phys. Rev. B* **1976**, *13*, 5188−5192.
(25) Hammer, B.; Nørskov, J. K. *Surf. Sci.* **1995**, *343*, 211−220.
(26) Hammer, B.; Nørskov, J. K. *Adv. Catal.* **2000**, *45*, 71−129.
(27) Henkelman, G.; Jónsson, H. *J. Chem. Phys.* **2000**, *113*, 9978−9985.
(28) Henkelman, G.; Uberuaga, B. P.; Jónsson, H. *J. Chem. Phys.* **2000**, *113*, 9901−9904.
(29) Sha, Y.; Yu, T. H.; Merinov, B. V.; Goddard, W. A. *ACS Catal.* **2014**, *4*, 1189−1197.
(30) Hilbrandt, N.; Martin, M. *J. Phys. Chem. B* **1999**, *103*, 4797−4802.
(31) Debecker, D. P.; Gaigneaux, E. M.; Busca, G. *Chem. - Eur. J.* **2009**, *15*, 3920−3935 and references therein.
(32) Ota, A.; Kunkes, E. L.; Kasatkin, I.; Groppo, E.; Ferri, D.; Poceiro, B.; Navarro Yerga, R. D.; Behrens, M. *J. Catal.* **2012**, *293*, 27−38.
(33) Frenkel, A. I.; Wang, Q.; Sanchez, S. I.; Small, M. W.; Nuzzo, R. G. *J. Chem. Phys.* **2013**, *138*, 064202.
(34) Frenkel, A. I. *Chem. Soc. Rev.* **2012**, *41*, 8163−8178.
(35) Canton, P.; Fagherazzi, G.; Battagliarin, M.; Menegazzo, F.; Pinna, F.; Pernicone, N. *Langmuir* **2002**, *18*, 6530−6535.
(36) Sandoval, M. J.; Bell, A. T. *J. Catal.* **1993**, *144*, 227−237.
(37) Sinha, N. K.; Neurock, M. N. *J. Catal.* **2012**, *295*, 31−44.
(38) Xin, H.; Linic, S. *J. Chem. Phys.* **2010**, *132*, 221101−221104.
(39) İnoğlu, N.; Kitchin, J. R. *Phys. Rev. B: Condens. Matter Mater. Phys.* **2010**, *82*, 045414.

DOI: 10.1021/jacs.6b02247
J. Am. Chem. Soc. 2016, 138, 6805−6812